Machine learning-assisted extreme value statistics of anomalies in AlSi10Mg manufactured by L-PBF for robust fatigue strength predictions

G. Minerva [a], M. Awd [b], J. Tenkamp [b], F. Walther [b], S. Beretta [a,*]

[a] Politecnico di Milano, Department of Mechanical Engineering, via La Masa 1, 20156, Milano, Italy
[b] Technische Universität Dortmund, Chair of Materials Test Engineering, Baroper Straße 303, 44227, Dortmund, Germany

ARTICLE INFO

ABSTRACT

Traditional Extreme Value Statistics (EVS) applied to block maxima sampled anomalies of components produced by Laser-Powder Bed Fusion may produce important inaccuracies in the estimated characteristic defects. In fact, the typical presence of multiple defect types may significantly affect the fitted maxima distributions obtained from different sampling volumes. In this work, we show how the limitations of traditional EVS can be overcome by applying supervised machine learning (ML) algorithms to classify the defects before estimating the maxima distributions for each defect type. The ML-assisted EVS provided maxima distributions unaffected by the different sampling volumes. The obtained maxima distribution lead to robust estimates of exceedance curves and finally, by employing the Shiozawa curve, to robust fatigue strength predictions.

1. Introduction

Fatigue behavior of additively manufactured (AMed) components has been an important research topic for several years. Many studies showed the relationship between fatigue properties and typical Additive Manufacturing (AM) features, in particular for surface roughness and internal defects. Yadollahi and Shamsaei [1] provided an overview on the effect of defect and surface roughness on the fatigue strength of AM materials. Masuo et al. [2] evaluated the effect of Hot Isostatic Pressing (HIP) and polishing on the fatigue life of Ti6Al4V, by investigating the change in surface roughness and internal defect size. Pegues et al. [3] investigated the surface roughness and size effect on the fatigue life of Ti6Al4V. Barricelli et al. [4] improved the estimates of fatigue life of annealed Ti6Al4V by accounting for shielding effect and a more accurate measurement of surface roughness. Beretta et al. [5] correlated surface roughness and the size of defects at the origin of fracture for as-built AlSi10Mg. Lee at al. [6] investigated the variability of surface roughness across different locations on the build platform and its effect on fatigue behavior for an L-PBF 316L stainless steel. Sanaei and Fatemi [7] provided a comprehensive review on the effect of volumetric defects on fatigue behavior. Romano et al. [8] described the effect of the size of artificial and natural defects on fatigue strength of AlSi10Mg. Nezhadfar et al. [9] compared fatigue behavior for different Al-based alloys, quantifying the defects size at the origin of fracture. Teschke et al.

[10] validated a defect-based fatigue modeling on a titanium aluminide alloy, studying the defects at the origin of fracture. Sausto et al. [11] investigated the effect of defect type and size on the axial and torsional fatigue life of AlSi10Mg. The main conclusion is that also for AM materials a direct link exists between the maximum defect and fatigue life [12–14], which can be described by the well-known Kitagawa-Takahashi diagram [15]. In recent years, Machine Learning (ML) has also been successfully employed to investigate the influence of fault characteristics on the high-cycle fatigue performance of AMed alloys. ML models allow to overcome the frequent constraint given by the lack of data [16,17] and to account for the effect of post-processing [18], microstructure [19], and defect location, size and morphology [20,21]. In fact, physics-informed ML approaches overcome the constraints of classical fracture mechanics and predict the fatigue finite life of materials in the presence of defects with unparalleled precision [22,23] and with significant computational efficiency, thus reducing the cost of structural integrity qualification [24]. Whether a pure fracture mechanics approach or a ML method is employed to estimate fatigue life, paramount importance has to be given to properly identifying the size of the potential "killer" defect which dictates the fatigue life of a component. To this aim, several studies have been devoted to estimate the extreme defects starting from the internal defects' distribution obtained with X-ray micro-computed tomography (CT scan) [25]. CT scan has been widely employed on AM components thanks to its versatility and

---

* Corresponding author.
  E-mail address: stefano.beretta@polimi.it (S. Beretta).

Nomenclature

$\sqrt{\text{area}}$	Square root of the defect area (Defect size)	P_e	Exceedance probability
$\sqrt{\text{area}_i}$	Failure initiating defect size	P_f	Failure probability
$\sqrt{\text{area}_f}$	Defect size at failure	R	Load ratio
$\sqrt{\text{area}_{crit}}$	Critical defect size	S_{el}	Surface area of the equivalent ellipsoid
$\nabla_w E$	Gradient vector	V_{BM}	Block Maxima sampling volume
α	Learning rate	V_{el}	Volume of the equivalent ellipsoid
γ	Shape parameter of the GEVD	V_{ref}	Prospective material volume
$\Delta\sigma$	Fatigue strength (stress range)	$\hat{x}_p$	Characteristic defect
ΔK_i	Cyclic SIF at failure initiating defect	Y	Shape factor
Δw	Gradient		
μ	Location parameter of the GEVD	*Abbreviations*	
σ	Scale parameter of the GEVD		
a	Maximum semi-axis of the equivalent ellipsoid	AM	Additive Manufacturing
b	Medium semi-axis of the equivalent ellipsoid	AMed	Additively Manufactured
c	Minimum semi-axis of the equivalent ellipsoid	CT scan	X-ray micro-computed tomography
C	Coefficient of Paris-Erdogan curve	DT	Decision Tree
d'	Exponent of Shiozawa curve	EVS	Extreme Value Statistics
E	Cost function	EV	Extreme Value
F	Distribution function	GEP	Gas-Entrapped Porosity
h	Height of sampling disk	GEVD	Generalized Extreme Value Distribution
K'_f	Coefficient of Shiozawa curve	HCF	High-Cycle Fatigue
m	Exponent of Paris-Erdogan curve	HIP	Hot Isostatic Pressing
N_i	Number of cycles spent in crack initiation	L-PBF	Laser-Powder Bed Fusion
N_f	Number of cycles to failure	LEVD	Largest Extreme Value Distribution
N_p	Number of cycles spent in crack propagation	LoF	Lack-of-Fusion
p	Parameter for the approximated surface area of the equivalent ellipsoid	ML	Machine Learning
		NN	Neural Network
		SEM	Scanning Electron Microscope
$p_\%$	Percentile	SIF	Stress Intensity Factor

the possibility of obtaining a large volume of data with a relatively low cost and time investment [26]. Moreover, recent standards for the qualification of AM processes and components require the employment of CT scan for investigating material anomalies, together with fractographies after fatigue tests [27]. However, transferability between specimens and components remains an open point. The starting point for these investigations is that there is a well-known size-effect that needs to be taken into account to evaluate fatigue life through a suitable statistical modeling [28–30]. This size-effect relates maximum defect size and relevant volume: the larger the volume the higher the probability of finding a large defect. This is well described by Extreme Value Statistics (EVS), which has been successfully employed to estimate the maximum defects [31,51,32,33]. However, for AM materials, exponential or Gumbel probability charts tend to show complex plots, which is a typical indicator of different types of defects being sampled together [34,35]. This is not surprising, considering that, within non-HIPed AM components, three main defect typologies have been extensively described in the literature [36–40], namely: i) gas-entrapped porosity (GEP), ii) keyhole porosity, iii) lack-of-fusion (LoF). Recognition of defect typology was initially done with the identification of simple thresholds using features obtained with the most common CT scan post-processors [41,42]. However, supervised ML approaches have recently shown promising results in the automated identification of the defect typology. Poudel et al. [43] trained two machine learning algorithms on a set of pre-classified defect to perform automatic identification of defect's types. Ye et al. [44] used machine learning to improve defect classification on low resolution CT scan using information coming from high resolution CT scan performed on the same coupons. Vandecasteele et al. [45] evaluated the transferability of a defect classification algorithm for LoFs and keyhole porosity across different materials and for different process parameters. Altmann et al. [46] showed that supervised classification models perform significantly better than unsupervised models to correctly identify GEP, LoF and keyhole pores from binary images.

The aim of this paper is to apply supervised machine learning approaches in order to improve the estimated maxima defects distribution obtained with EVS by fitting distributions for each defect typology. In this way, it would be possible to properly capture the size-effect for each distribution and thus to improve fatigue strength predictions.

2. Materials and methods

The fatigue specimens used in this study were fabricated by laser-powder bed fusion (L-PBF). The specimens were manufactured using an SLM 280HL v1.0 system equipped with two 400 W Yttrium fibre lasers working in parallel in a build chamber that measures 280x280x350 mm^3 (SLM Solution Group AG). The build chamber was flooded with argon to reach oxygen levels lower than 0.2% during the printing process. The printing parameters were as follows: beam power P = 350 W, hatch distance h = 0.13 mm and scan speed v = 1650 mm/s. The selected layer thickness was t = 50 μm and produced an energy density of 32.63 J/mm^3. The building platform was pre-heated up to 150 °C. The scan strategy adopted stripes rotated by 67° after each layer and the scanning order was two contours, followed by the hatch scanning. AlSi10Mg powder, produced by ECKA Granules, was characterized by a mean granule size of 37 μm, $D_{10} = 21$ μm and $D_{90} = 65$ μm with a flowability of 80 s/50 g. Before separating the specimens from the building platform, the build job was subjected to an artificial ageing heat treatment (200 °C for 4 hours).

Fig. 1 shows the specimens dimensions: the gauge section had diameter equal to 9.6 mm and length equal to 5 mm. An overstock of 0.2 mm on all surfaces and a 30 mm longer lower part were considered to allow machining operations. All the specimens were printed in the vertical (z) direction, i.e. with the loading axis corresponding to the building direction.
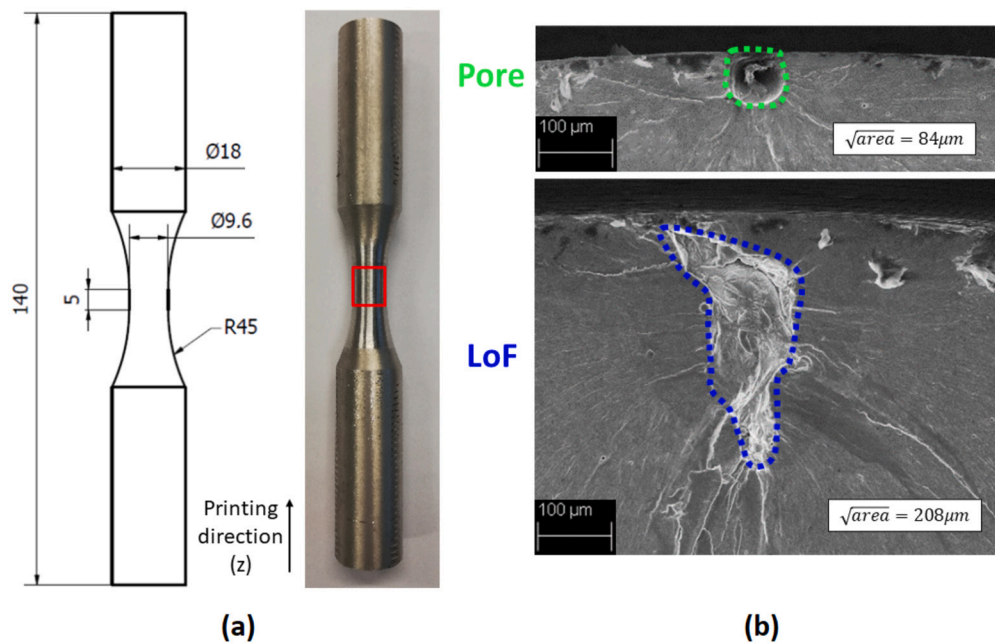
Fig. 1. (a) HCF specimen geometry (all dimensions in [mm]) with two exemplary defects at the origin of fracture: (b) a gas-entrapped pore and a lack-of-fusion. Adapted from [11].

2.1. Fatigue tests

Fatigue tests were conducted on a servo-hydraulic MTS Landmark testing machine with a maximum force capacity of 100 kN. The tests were carried out in force control at 25 Hz under completely reversed loading conditions (i.e. with a load ratio $R = 1$). Specimens that survived $5 \cdot 10^6$ cycles were considered run-outs and retested at a higher load. More details on the specimens and the fatigue tests can be found in [11].

2.2. Fracture analysis

After the fatigue tests, the specimens were subjected to ultrasonic cleaning in ethanol to remove dust and particles from the fracture surfaces. The fracture surfaces were subsequently analyzed with a stereo microscope and with a Zeiss EVO 50 Scanning Electron Microscope (SEM). The defect size expressed as $\sqrt{area}$ of the defect projected on the xy plane (i.e.: perpendicular to the loading direction) was measured with the software ImageJ.

2.3. X-ray micro-computed tomography

After the fatigue tests, the grip ends of the HCF specimens were investigated by means of CT scan to reveal the volumetric anomalies induced by the manufacturing process. The volume to be investigated was selected considering the indications of ESA standards ECSS-Q-ST-70-80C [27] for qualification of AM processes, which requires as a minimum the scan of the gauge section of 24 axial fatigue specimens. Considering slightly larger specimens than the one employed in this study, with a diameter equal to 10 mm and a 20 mm gauge length, the prospective volume to be investigated was approximately 38,000 mm^3. The same volume was obtained by cutting cylindrical portions with height equal to 30 mm from five grip ends of the HCF specimens, having a diameter of 18 mm. The tomograph employed was a Zeiss Metrotom 1500, while the scanning parameters were: detector pixel pitch equal to 113 μm, focal spot size of 30 μm, voltage of 210 kV, magnification of x9.3, resulting in a voxel size of 15 μm. The rather large voxel size was selected in order to easily analyze large material volumes while retaining a good enough description of the defects' features.

The volumetric defects population was obtained using VGStudio Max software version 3.4.2, employing the EasyPore algorithm, which allows to obtain sub-voxel precision for the segmentation [47]. A relative difference of 80% on the threshold, set equal to the iso-value 60 between air and material peaks of the intensity histogram, was found to lead to a good identification and shape reconstruction of the defects. These values were iteratively obtained by visually checking the identified anomalies on a small material volume. For CT scan, the minimum defect size that can be accurately identified is typically in the order of three times the voxel size, thus a threshold on the minimum defect size was set to 50 μm. Fig. 2 shows the defects typologies revealed by the analysis: Gas Entrapped Porosity (GEP) or pores, cluster of pores, Lack-of-Fusion (LoF).

2.4. Supervised machine learning

Supervised machine learning requires pre-classified data to help reveal the entangled relationship between samples in a specific domain, i.e. defect features for categorization (GEP, LoF, etc.). A wide range of techniques exists to perform this task. The common ground here is that the data needs to be pre-classified and is then given as input to the algorithm as a training data set. The pre-classification performed on the training data set is used by the algorithm to automatically perform the intended task on new data sets [48]. Supervised machine learning can be implemented as a stand-alone element or as part of a larger or automated artificial intelligence workflow. It can also follow the implementation of an unsupervised machine learning algorithm. Unsupervised learning techniques do not need any information about the classes of the features used for the training and they allow to solve the clustering problem and then provide the input for the next step in the workflow [49]. Supervised machine learning can be distinguished from reinforcement learning, because for supervised machine learning there is a direct error measure between the prediction and the target in every iteration, which tells whether the loss function is satisfied. Unlike reinforcement learning, there is no rewarded agent, but a classical gradient descent rule is evaluated continuously:
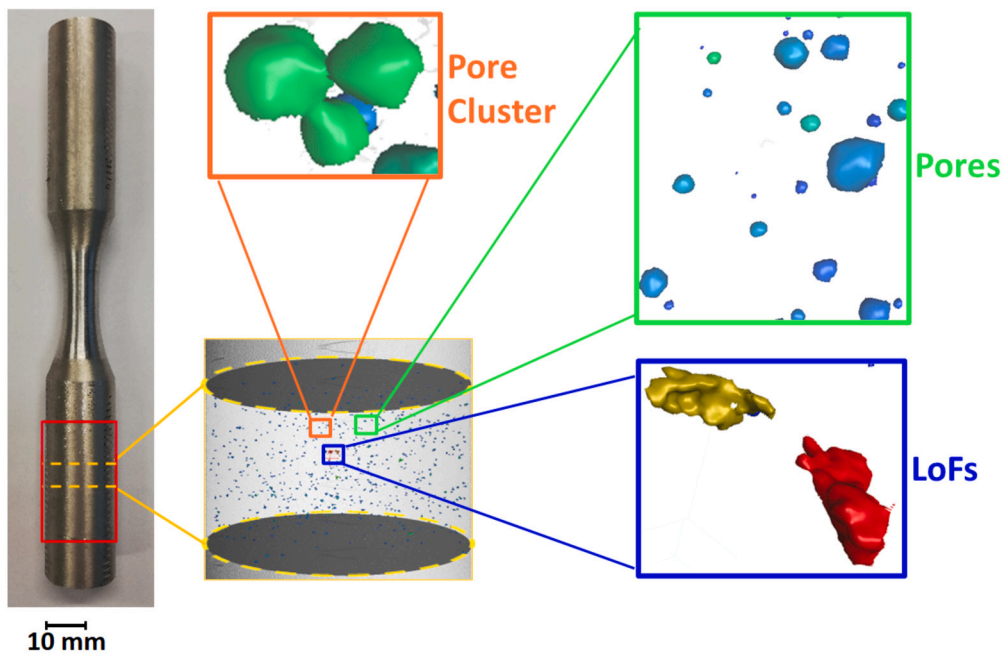
$$\Delta w = \alpha \nabla_w E \tag{1}$$

Fig. 2. Schematics of the CT scan of the grip portions of the HCF specimens (red region) and examples of volumetric defects obtained from the analysis (not to scale).

where α is the learning rate, E is the cost function, and $\nabla_w E$ is the gradient vector. Although applying the concept of supervised machine learning is relatively straightforward, it requires large training data sets. However, the recent development of high throughput CT scan provides large data for the classification problem of defects. In this work, we decided to use the neural network (NN) classifier of Matlab, which is a multilayered perceptron. We applied backward propagation in the training stage by feeding the network the class information of the features we obtained from CT scan analysis. The training process was automated and employed bayesian optimization over 100 iterations. In this process, the weights and coefficients of the neurons across all layers were optimized for the given training data set. We also applied a decision tree (DT) in Matlab, which is a tree-like prototype of choices with a grade of possible significance, in support of the neural network. Although it has been used historically as a decision-making tool, we employed the decision tree as a classification algorithm following the work of Poudel et al. [43]. For the decision tree, arrowheads distribute information to nodes and each node may be split into sub-nodes based on graded functions. The decision tree terminated with leaves showing the final results of the classification [48].

3. Results

3.1. Block maxima sampling

Defect size can be expressed by the $\sqrt{area}$ parameter [50], which refers to the square root of the area of the defect projected onto a plane perpendicular to the applied stress. VGStudio Max allows to directly extract the defect areas projected on the xy, xz, yz planes of the xyz reference system [47]. Therefore, with proper alignment of the scanned component, it's a trivial process to obtain the defect sizes for all the defects revealed by CT-scan analyses. The defect data can be subsequently analyzed with the statistics of extremes by performing Block Maxima (BM) sampling [51]. In this work, BM sampling was carried out on the complete set of defect data by piling up the five volumes of the grip ends of the specimens and then dividing the obtained cylinder in disks of fixed height h, each with sampling volume $V_{BM} = h \cdot \pi \cdot r^2$. For each sampling disk, the largest defect was recorded and the obtained maxima were fitted with the Generalized Extreme Value Distribution (GEVD), which has distribution function [52]:

$$F(x) = \begin{cases} \exp\left(-\left(1 + \gamma \cdot \dfrac{x - \mu}{\sigma}\right)^{-\frac{1}{\gamma}}\right) & \text{for } \gamma \neq 0 \\ \exp\left(-\exp\left(-\dfrac{x - \mu}{\sigma}\right)\right) & \text{for } \gamma = 0 \end{cases} \quad (2)$$

Where:

- γ is the shape parameter.
- μ is the location parameter.
- σ is the scale parameter.

For $\gamma = 0$ we have a Type I GEVD, also known as Gumbel distribution or Largest Extreme Value Distribution (LEVD).

Different sampling volumes were considered for the analysis, simply by changing the height h of the sampling disks. Fig. 3 shows four Extreme Value Distributions obtained for increasing values of sampling volume: $V_{BM} = 25.5$ mm^3, $V_{BM} = 127$ mm^3, $V_{BM} = 520$ mm^3 and $V_{BM} = 1270$ mm^3. The distributions' parameters, reported in Table 1, were fitted using maximum likelihood method for GEVD [53] and moments method for the LEVD [54]. Maximum likelihood is a method in which the distribution parameters are obtained by maximizing the probability that the sample data belongs to the selected distribution. Moments method provides estimates of the distribution parameters using the average and the standard deviation of the sample data. It minimizes the difference between the observed moments of the sample data and the analytical moments of the distribution. From Fig. 3, it's possible to see how the maxima defect distribution changes significantly with the sampling volume:

- for $V_{BM} = 25.5$ mm^3 the distribution is a Type II GEVD (Fréchet distribution) which follows closely the data for small values of $\sqrt{area}$, while it doesn't fit properly the largest values of $\sqrt{area}$.
- for $V_{BM} = 127$ mm^3 the distribution is still a Type II GEVD, with a higher value of γ. In this case, the distribution well fit all the data.
- for $V_{BM} = 520$ mm^3 the distribution has become a LEVD that provides a good fit for the maxima. However, any information on the change of shape moving from smaller defects to larger defects is lost.
- for $V_{BM} = 1270$ mm^3 the distribution is still a LEVD, with a slightly higher slope.

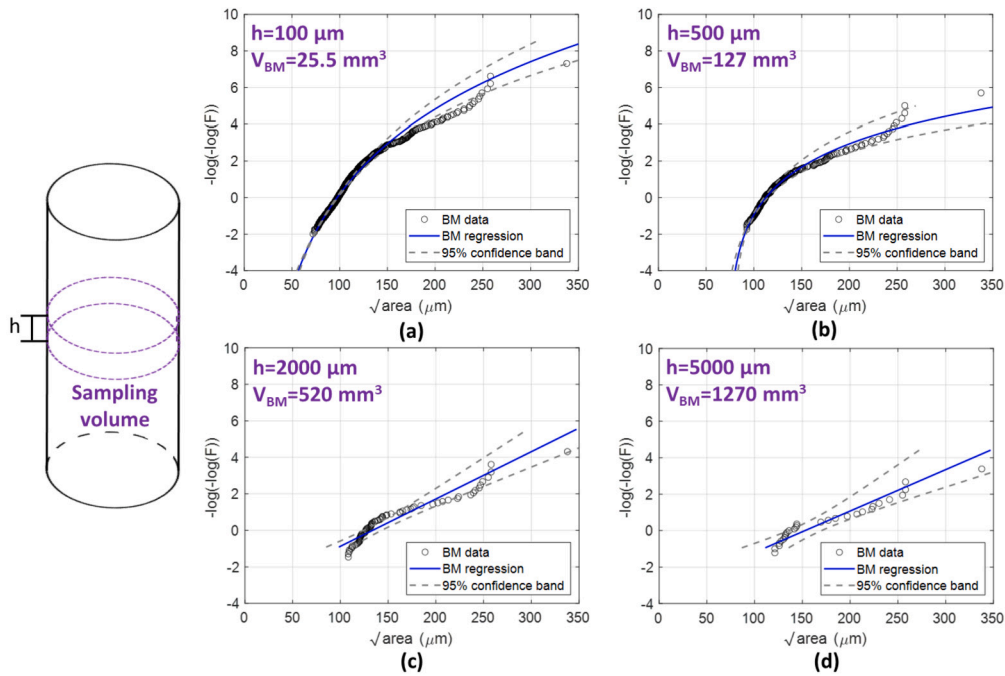**Fig. 3.** Extreme value distributions for different sampling disk volumes: (a) GEVD with $V_{BM} = 25.5$ mm^3 ; (b) GEVD with $V_{BM} = 127$ mm^3; (c) LEVD with $V_{BM} = 520$ mm^3; (d) LEVD with $V_{BM} = 1270$ mm^3.

Table 1
Estimated parameters of EV distributions obtained on sampling volumes V_{BM} =25.5, 127, 500, 1270 mm^3.

V_{BM} [mm^3]	γ	μ [μm]	σ [μm]
25.5	0.1661	97.25	13.89
127	0.3919	112.39	15.83
520	0	133.73	38.59
1270	0	152.65	44.02

The severe effect of the sampling volume on the fitted Extreme Value Distributions may be evidenced by estimating characteristic defects for different reference volumes V_{ref}. The characteristic defect $\tilde{x}_p$ on V_{ref} having exceedance probability (1-p)%, corresponding to the pth percentile, may be estimated with [35,53]:

$$\hat{x}_p = \begin{cases} \mu + \dfrac{\sigma}{\gamma} \cdot \left(\left(-\log\left(p^{\frac{V_{BM}}{V_{ref}}} \right) \right)^{-\gamma} - 1 \right) & \text{for GEVD} \\ \mu - \sigma \cdot \log\left(\dfrac{V_{BM}}{V_{ref}} \right) - \sigma \cdot \log\left(-\log(p) \right) & \text{for LEVD} \end{cases} \quad (3)$$

In Table 2 we considered three characteristic defects for each fitted distribution and reference volume: a lower bound defect having 90% exceedance probability (p_{10}), the average defect (p_{50}) and an upper bound defect having 10% exceedance probability (p_{90}). It's evident how the estimated characteristic defects drastically change with the sampling volume, in particular for very small reference volumes V_{ref}. BM sampling performed with large sampling volumes ($V_{BM} = 520$ mm^3, $V_{BM} = 1270$ mm^3) leads to estimated characteristic defects on $V_{ref} = 5042$ mm^3 with very small values. However, for smaller sampling volumes ($V_{BM} = 25.5$ mm^3, $V_{BM} = 127$ mm^3) the estimated characteristic defects are significantly bigger. On the other hand, for larger reference volumes, e.g. $V_{ref} = 2000$ mm^3, the estimated lower bound (p_{10}) and average defects (p_{50}) do not differ as much among the EV distributions, while the upper bound defects (p_{90}) are significantly apart.

The differences evidenced between the maxima distributions may be attributed to the presence of different types of defects. In fact, each

Extreme Value Distribution is the results of maxima data from different defect populations. This effect is clearly depicted by Fig. 4, where defect size as $\sqrt{\text{area}}$ is reported alongside compactness and sphericity parameters for all defects. Compactness and sphericity were selected as simple shape descriptors for the defects, since they are directly provided by VGStudio Max, and are defined as:

$$Compactness = V_{defect}/V_{sphere,circumscibed} \quad (4)$$

$$Sphericity = S_{sphere,equivolume}/S_{defect} = \sqrt[3]{36\pi \cdot V_{defect}^2}/S_{defect} \quad (5)$$

Where V is the volume, S is the area of the external surface, the circumscribed sphere is the sphere circumscribed to the defect and the equivolume sphere is the sphere having the same volume as the defect. Defects sampled with BM are highlighted with red crosses and refer to sampling volume $V_{BM} = 25.5$ mm^3 for Fig. 4(a) and to $V_{BM} = 520$ mm^3 for Fig. 4(b). Independently of the sampling volume, two distinct populations appear to be sampled with BM: defects with low compactness (<0.25) and sphericity (<0.8), presumably pore clusters and LoFs highlighted in orange and blue, and defects with high compactness (>0.25) and sphericity (>0.8), presumably pores highlighted in green.

3.2. Defect classification with supervised machine learning algorithms

The manual separation of defects revealed by CT scan into the observed classes is an extremely inefficient task to be performed individually for each defect. Recently, supervised machine learning algorithms, such as neural network and decision tree, have been successfully employed on Ti6Al4V specimens realized by L-PBF for the automatic classification of pores, LoFs and keyhole porosity. Following the procedure described in [43], 1107 defects were individually classified: pores, clusters and LoFs.

Fig. 5 shows defect size, compactness and sphericity of the hand-picked defects. As expected, pores lie in the region with high sphericity and compactness. The regions of cluster of pores and LoFs significantly overlap. For this reason, pore clusters were assimilated into the LoFs class and only two classes were employed for the training of defect classification algorithms: pores and LoFs. Following the work of Poudel et al. [43], several shape descriptors were calculated for all the de-

Table 2
Estimated percentiles p_{10}, p_{50}, p_{90} on V_{ref} =50, 500, 1000, 2000 mm³ from EV distributions obtained on sampling volumes V_{BM} =25.5, 127, 500, 1270 mm³.

| V_{ref} 50 mm³	p_{10} [μm]	p_{50} [μm]	p_{90} [μm]	V_{ref} 500 mm³	p_{10} [μm]	p_{50} [μm]	p_{90} [μm]
V_{BM} = 25.5 mm³	95	113	150	V_{BM} = 25.5 mm³	133	159	213
V_{BM} = 127 mm³	92	104	140	V_{BM} = 127 mm³	122	152	239
V_{BM} = 520 mm³	11	58	130	V_{BM} = 520 mm³	100	146	219
V_{BM} = 1270 mm³	-26	26	109	V_{BM} = 1270 mm³	75	128	211
V_{ref} 1000 mm³	p_{10} [μm]	p_{50} [μm]	p_{90} [μm]	V_{ref} 2000 mm³	p_{10} [μm]	p_{50} [μm]	p_{90} [μm]
V_{BM} = 25.5 mm³	148	177	237	V_{BM} = 25.5 mm³	164	197	264
V_{BM} = 127 mm³	137	177	291	V_{BM} = 127 mm³	158	209	359
V_{BM} = 520 mm³	127	173	246	V_{BM} = 520 mm³	154	200	273
V_{BM} = 1270 mm³	105	158	241	V_{BM} = 1270 mm³	136	189	272
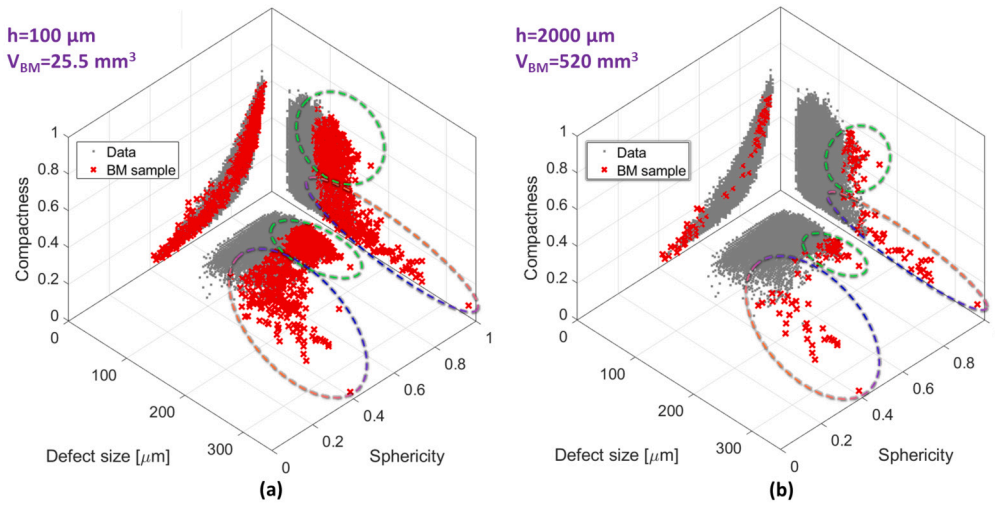
Fig. 4. Defect size, compactness and sphericity parameters of all the defects revealed by CT scan, with defects sampled with Block Maxima highlighted with red crosses for Sampling volume: (a) V_{BM} = 25.5 mm³; (b) V_{BM} = 520 mm³. Green ellipses encircle to possible pores, while blue and orange ellipses refer to possible LoFs and pore clusters.
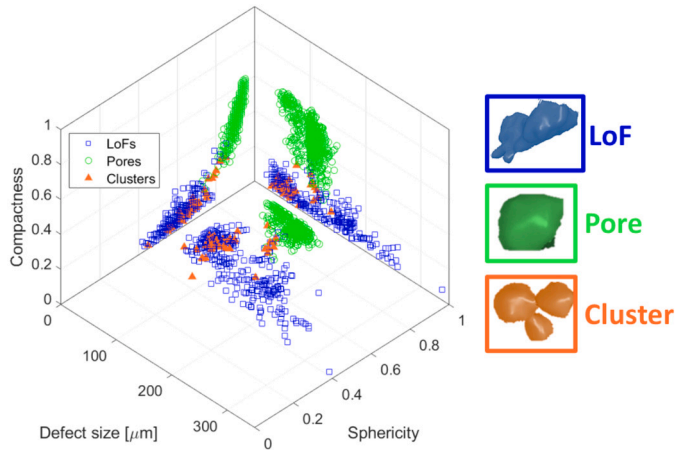

Fig. 5. Defect size, Compactness and Sphericity of identified pores, pore clusters and lack-of-fusions.

fects. However, since the defects features were directly obtained from VGStudio Max, a different approach was employed for the equivalent ellipsoid. In this work, the equivalent ellipsoid was defined as the ellipsoid having the same projected areas as the defect. The axes a, b, c where calculated as:

$$
\begin{cases}
a = max \left(\sqrt{\frac{1}{\pi} \cdot \frac{\mathrm{area}_{xy} \cdot \mathrm{area}_{yz}}{\mathrm{area}_{xz}}}, \sqrt{\frac{1}{\pi} \cdot \frac{\mathrm{area}_{xz} \cdot \mathrm{area}_{yz}}{\mathrm{area}_{xy}}}, \sqrt{\frac{1}{\pi} \cdot \frac{\mathrm{area}_{xz} \cdot \mathrm{area}_{yz}}{\mathrm{area}_{xy}}} \right) \\
b = \left(\sqrt{\frac{1}{\pi} \cdot \frac{\mathrm{area}_{xy} \cdot \mathrm{area}_{yz}}{\mathrm{area}_{xz}}}, \sqrt{\frac{1}{\pi} \cdot \frac{\mathrm{area}_{xz} \cdot \mathrm{area}_{yz}}{\mathrm{area}_{xy}}}, \sqrt{\frac{1}{\pi} \cdot \frac{\mathrm{area}_{xz} \cdot \mathrm{area}_{yz}}{\mathrm{area}_{xy}}} \right) \cap \bar{a} \cap \bar{c} \\
c = min \left(\sqrt{\frac{1}{\pi} \cdot \frac{\mathrm{area}_{xy} \cdot \mathrm{area}_{yz}}{\mathrm{area}_{xz}}}, \sqrt{\frac{1}{\pi} \cdot \frac{\mathrm{area}_{xz} \cdot \mathrm{area}_{yz}}{\mathrm{area}_{xy}}}, \sqrt{\frac{1}{\pi} \cdot \frac{\mathrm{area}_{xz} \cdot \mathrm{area}_{yz}}{\mathrm{area}_{xy}}} \right)
\end{cases}
\tag{6}
$$

so that $a \geq b \geq c$.

The volume of the ellipsoid V_{el} was thus obtained with the formula:

$$
V_{el} = \frac{4}{3} \pi abc
\tag{7}
$$

The surface of the ellipsoid S_{el} was calculated with the approximated formula:

$$
S_{el} = 4\pi c^2 \sqrt[p]{\frac{(ab)^p + (ac)^p + (bc)^p}{3}}
\tag{8}
$$

where $p = 1.6075$ was used, leading to a negligible error (<1%).

The complete set of features employed for the classification was as follows:

- Compactness (see Equation (4));
- Sphericity (see Equation (5)).
- Maximum axis of the equivalent ellipsoid;
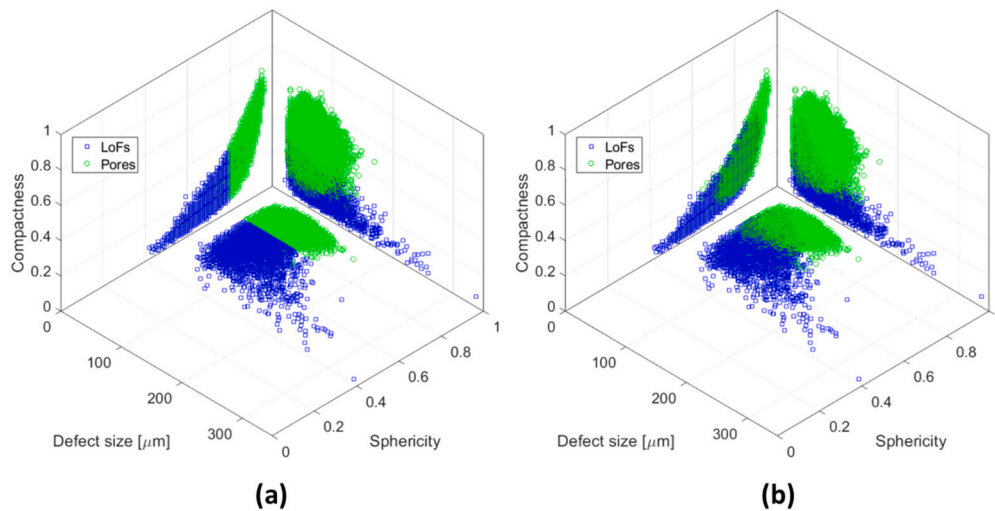- Sparseness: Ratio between the volume of the defect and the volume of the equivalent ellipsoid.

Fig. 6. Defect size, Compactness and Sphericity of identified Pores and Lack-of-Fusions with: (a) Decision Tree; (b) Neural Network.

- Roundness: Ratio between the diameter of the sphere having the same volume as the defect and the maximum axis of the equivalent ellipsoid;
- Aspect Ratio: Ratio between minimum and maximum axes of the equivalent ellipsoid;
- Elongation: Ratio between medium and maximum axes of the equivalent ellipsoid;
- Extent: Ratio between the volume of the defect and the volume of the bounding box;
- Ellipsoidity: Ratio between the surface of the equivalent ellipsoid and the surface of the defect.

The two selected classification algorithms, neural network and decision tree, were trained with five-fold cross validation on 70% of the 1107 hand-picked defects, using all the shape descriptors as input. The remaining 30% were used for testing of the algorithms. The structure of the neural network in terms of number of layers, number of neurons per layer and of the activation algorithm were selected by the optimization performed in Matlab using a grid search optimizer with 10 divisions with a 3600 s time limit. The optimization resulted in a neural network consisting of 3 layers with neurons as follows: first layer with 13 neurons, second layer with 13 neurons and third layer with 2 neurons. We used a Bayesian optimizer for the decision tree, with an acquisition function for 30 iterations without a training time limit. The obtained accuracies were as follows:

- DT, with 98.8% training accuracy and 99.1% testing accuracy.
- NN, with 99.1% training accuracy and 98.8% testing accuracy.

We then used the constructed contingent functions of the classification algorithms on the complete set of data, to classify the defects as either pores or LoFs. Fig. 6 shows all the defects classified by the different algorithms: blue squares represent LoFs, while green circles represent Pores. The algorithms separated the defects as:

- DT: 123948 Pores; 20355 LoFs.
- NN: 106055 Pores; 38248 LoFs.

Despite the significant differences in the relative numbers of pores and LoFs, the largest defects (size>100 μm) of the two populations coincided. This was extremely promising, since it should lead to negligible differences between the maxima distributions after BM sampling.

Table 3
Percentage of sampled pores and LoFs from Neural Network classification in Extreme Value distributions.

V_{BM} [mm^3]	Pores		LoFs	
	n_{pores}	pores%	n_{LoFs}	LoFs%
127	1193	79.6	306	20.4
256	205	68.6	94	31.4
520	33	44.6	41	55.4
1270	13	44.8	16	55.2

4. Discussion

4.1. Analysis of BM sampled data

After performing the defect classification, it was possible to determine the effect of the presence of different defects types onto the fitted EV distributions for the different sampling volumes defined in Section 3.

Fig. 7 shows the fitted EV distributions with the sampled maxima divided into the pores and LoFs classified with the neural network algorithm. Table 3 reports the number and percentage of pores and LoFs for the different sampling volumes. The differences between the EV distributions may then be attributed to the different ratio of defects extracted out of the two defect populations:

- for small sampling volumes the ratio of LoFs and clusters to pores is quite low, thus the smaller maxima (pores) have a higher weight on the fitted GEVD, which can not follow the larger maxima (LoFs).
- for large sampling volumes the ratio of LoFs and clusters to pores significantly increases, hence why the fitted LEVD follows better the larger maxima.

4.2. ML-assisted BM sampling

After the classification, BM sampling was performed separately on the two classes, with the same procedure described in Section 3.

Fig. 8 shows the LEV distributions for pores and LoFs classified with neural network algorithm for different sampling volumes, while the fitted parameters are reported in Table 4. In order to sample the maxima out of at least 20 defects, the minimum sampling volume was increased to 127 mm^3. The lower tail of the LoFs' LEV distributions is not fully captured by the fitted parameters and the smaller maxima defects seems to follow a slope similar to the one of pores distribution. This is a possible indicator that the defects below $\sqrt{area} = 100$ μm are all pores clusters, which share the same density as the pores. However, it is im-
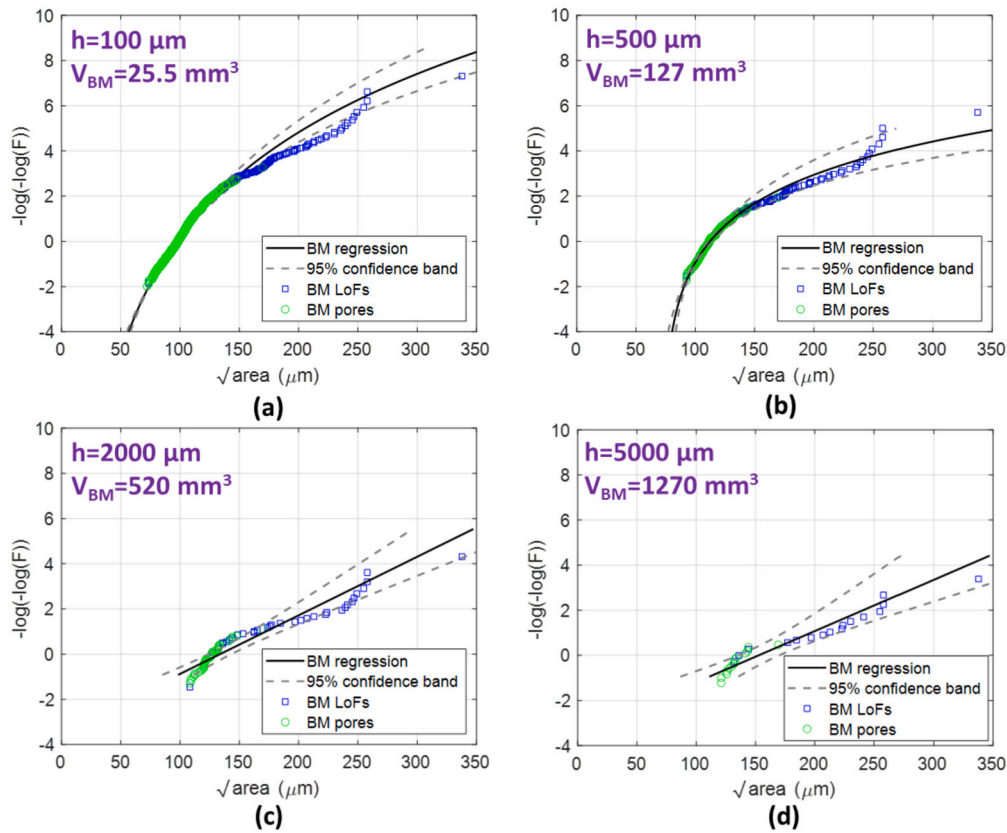
Fig. 7. Sampled pores and LoFs from Neural Network classification in Extreme Value distributions with sampling disk volumes V_{BM}: (a) 127 mm^3; (b) 256 mm^3; (c) 520 mm^3; (d) 1270 mm^3.

Table 4
Estimated parameters of EV distributions for pores and LoFs classified with Neural Network.

V_{BM} [mm^3]	Pores		LoFs	
	μ [μm]	σ [μm]	μ [μm]	σ [μm]
127	109.30	9.20	87.97	37.58
256	115.28	8.98	99.20	43.31
520	120.07	8.87	114.40	46.92
1270	127.59	9.05	135.57	52.80

Table 5
Estimated percentiles p_{10}, p_{50}, p_{90} on $V_{ref} = 50$ and 2000 mm^3 from Pores and Lack-of-Fusions LEVDs, sampled after defect classification with Neural Network algorithm.

	Pores			LoFs		
	p_{10} [μm]	p_{50} [μm]	p_{90} [μm]	p_{10} [μm]	p_{50} [μm]	p_{90} [μm]
V_{BM}	$V_{ref} = 50$ mm^3					
127 mm^3	93	96	121			
256 mm^3	93	96	121			
520 mm^3	92	95	119			
1270 mm^3	90	94	118			
V_{BM}	$V_{ref} = 2000$ mm^3					
127 mm^3	127	138	155	160	205	276
256 mm^3	126	137	154	152	204	286
520 mm^3	125	135	152	139	195	284
1270 mm^3	124	135	152	114	177	276

portant to underline that the larger maxima (LoFs) are well described by all fitted LEVDs and that clusters of pores may act as a single defects rather than as individual pores.

Table 5 reports the estimated characteristic defects onto $V_{ref} = 50$ mm^3 and $V_{ref} = 2000$ mm^3 for the pores and LoFs distributions. It is possible to see how the estimates are now stable with different sampling volumes. No estimates are reported for $V_{ref} = 50$ mm^3 from LoFs distribution since the number of LoFs on such a small reference volume would be too few to be correctly estimated with the Gumbel distribution.

5. ML-assisted extreme value statistics

The results have shown how the traditional EVS did not provide robust estimates. Fig. 9(a) shows the current routine to estimate maxima defect distributions from CT scan data using EVS [7,34,51,55,56]:

1. Specimens are subjected to CT scan.
2. Internal defects are revealed with dedicated post-processors.
3. BM sampling is performed onto the defects.
4. EVS is employed to fit the maxima defect distributions and make predictions onto relevant volumes.

Following the results obtained with the stabilized Extreme Value distributions after Machine Learning-assisted defect classification, the authors propose a new way to estimate defect distributions from CT scan of AMed components as shown in Fig. 9(b):

1. Specimens are subjected to CT scan.
2. Internal defects are revealed with dedicated post-processors.
3. A selection of defects representative of different types are individually classified.
4. ML algorithms are trained using the identified defects and then employed to classify all the defects revealed by CT scan.
5. BM sampling is performed separately onto the different defects types.
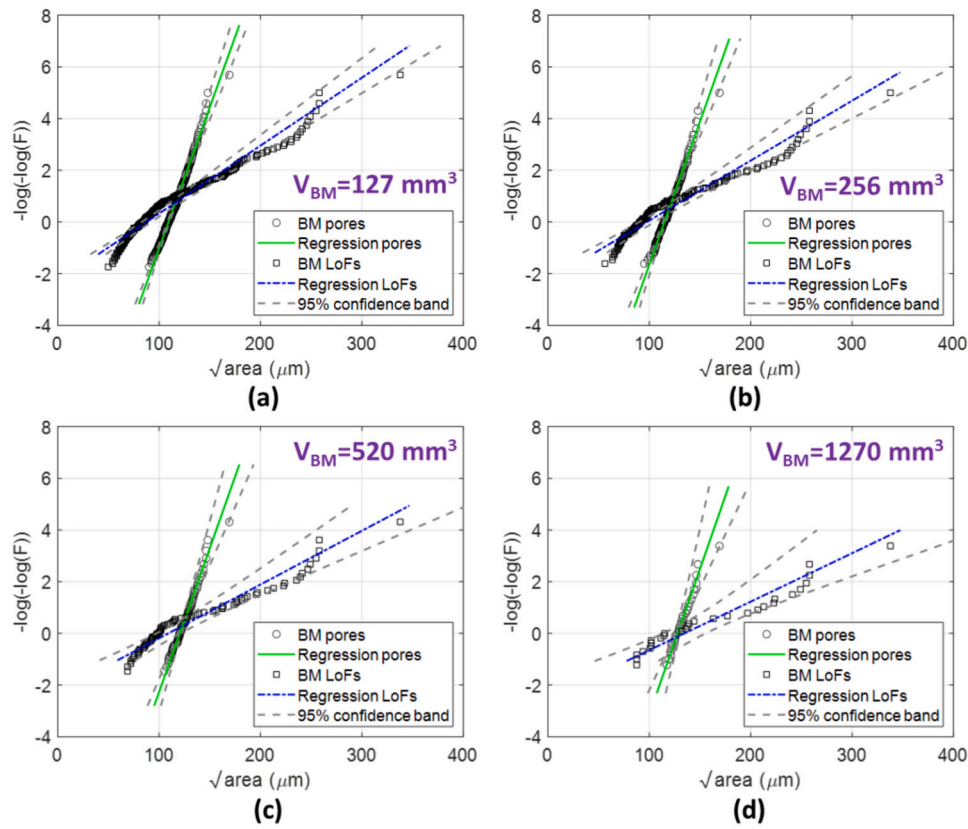
Fig. 8. Largest Extreme Value distributions of pores and LoFs for Neural Network classification algorithm with sampling disk volumes V_{BM}: (a) 127 mm^3; (b) 256 mm^3; (c) 520 mm^3; (d) 1270 mm^3.
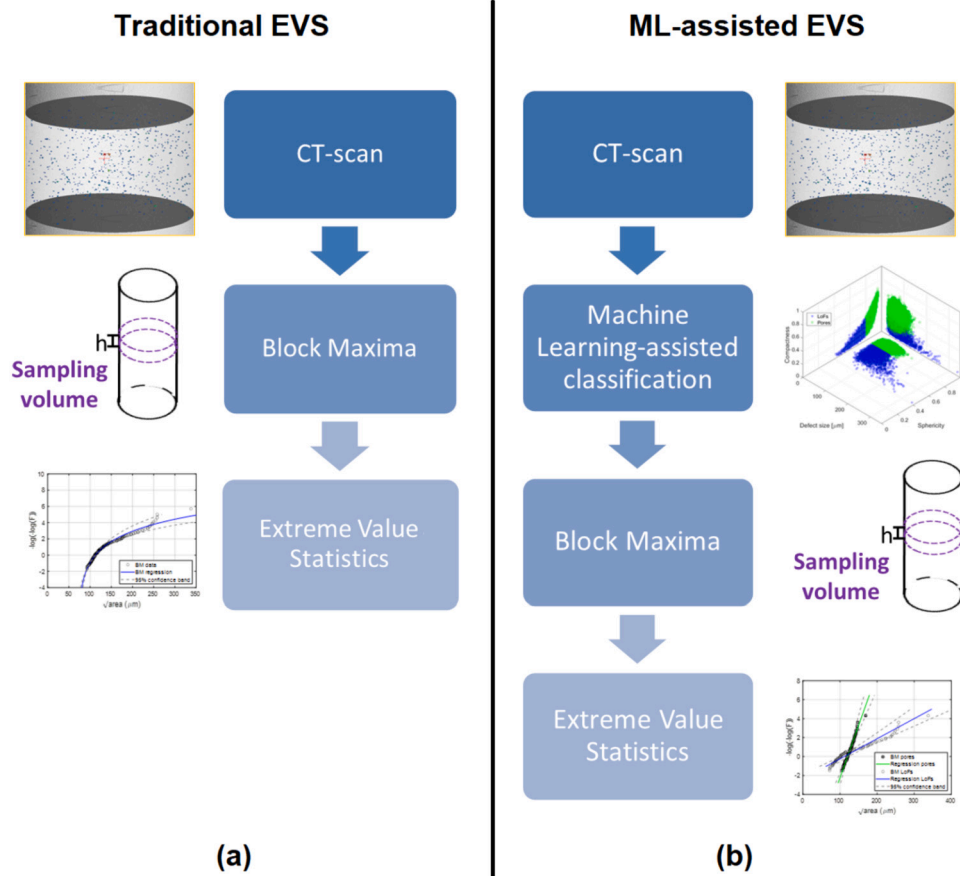

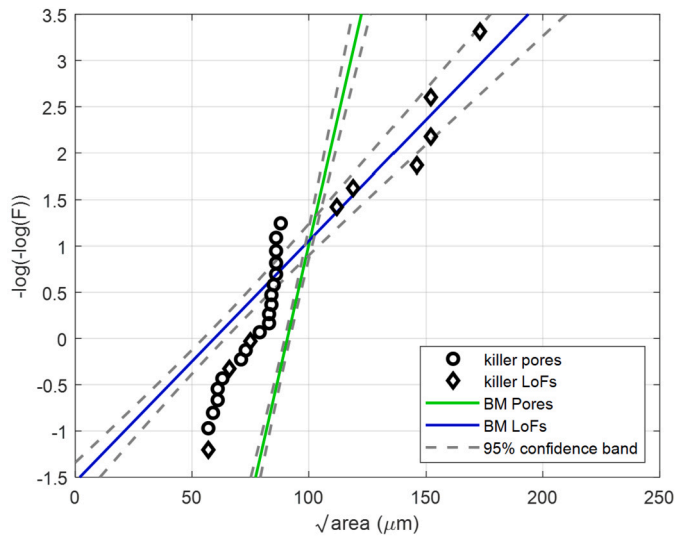**Fig. 9.** Extreme Value Statistics on CT scan data: (a) current route; (b) proposed new route.

Fig. 10. Comparison between killer defects observed on fracture surfaces from [11] and estimated maxima distributions from CT scan data obtained using BM with a sampling volume of 127 mm^3 and transformed to the occurrence volume by Eq. (9).

6. EVS is employed to fit the maxima defect distributions and make predictions onto relevant volumes for each defect type.

An important limitation to consider is that the machine learning algorithm is valid only for the specific combination of material, processing parameters and CT measurement setup. A change in one of these aspects will require to perform the complete training procedure of ML models. It is also important to underline that the authors do not intend to propose a general recipe for the analysis, because different anomalies can have different effects on material properties (e.g.: porosity can have a significant effect on toughness and static resistance).

Once the anomaly distribution on the V_{BM} sampling volume has been obtained, then the prospective distribution of the maximum defect on a reference volume V_{ref} can be obtained as:

$$F(x)_{max,V_{ref}} = [F(x)_{max,V_{BM}}]^n \qquad (9)$$

where $n = \frac{V_{ref}}{V_{BM}}$ is the so called *return period* of the largest defect in V_{ref}.

Applying Eq. (9) to the two different distributions for pores and LoFs to the prospective occurrence volume for the axial fatigue specimens, it is then possible to estimate the distribution of defects at the origin of fatigue failures. The comparison with the results of the test campaign on axial and torsional specimens is shown in Fig. 10, where it can be seen that the estimated distributions for the two different anomaly types are quite close to the experimental results.

6. Application to fatigue assessment

6.1. Simple model for effect of defects on fatigue life

It has been extensively proved how volumetric anomalies may act, and thus be modeled, as short cracks [7,8,11,32,57,58]. For unified assessment of stress amplitude and defects ($\sqrt{area}$), a relevant model is the Shiozawa curve [59], successfully employed on Al-Si alloys by Tenkamp et al. for cast AlSi7Mg and AlSi10Mg as well as L-PBF AlSi10Mg [60,61]. The main conditions on the validity of Shiozawa are that: i) the fatigue behavior is crack propagation dominated ($N_p \gg N_i$); ii) the failure-initiating defects $\sqrt{area_i}$ are relatively small compared to the final fatigue crack size at failure $\sqrt{area_f}$ ($\sqrt{area_f} \gg \sqrt{area_i}$). Hereby, the Paris-Erdogan law is integrated from the initial defect size $\sqrt{area_i}$ to fatigue crack size at failure $\sqrt{area_f}$ resulting in the following equations:

Table 6
Estimated parameters of Shiozawa curve for the investigated L-PBF AlSi10Mg.

K_f'	$1/d'$
42.428	7.9662

$$\Delta K_i = \left[\frac{C(m-2)}{2}\right]^{-1/m} \cdot \left(\frac{N_f}{\sqrt{area_i}}\right)^{-1/m} \qquad (10)$$

$$\Delta K_i = K_f' \cdot \left(\frac{N_f}{\sqrt{area_i}}\right)^{d'} \qquad (11)$$

Comparable to S-N diagrams, the cyclic stress intensity factor at the failure-initiating defect ΔK_i (y axis) is plotted against the quotient of number of cycles to failure N_f and failure-initiating defect size $\sqrt{area_i}$ (x axis) according to Equation (11) and the results appear in a double logarithmic diagram as a straight line, analogous to the common Woehler lines. ΔK_i is estimated by using the Murakami approach for short cracks [57]:

$$\Delta K_i = \Delta\sigma \cdot Y \cdot \sqrt{\pi \cdot \sqrt{area_i}} \qquad (12)$$

Where the shape factor Y is equal to 0.65 for surface defects and to 0.5 for volumetric (internal) defects.

The fatigue behavior for the investigated L-PBF AlSi10Mg material was characterized by Woehler (Fig. 11a) and Shiozawa diagrams (Fig. 11b). Hereby, the coefficient of determination (r2) is significantly better for Shiozawa curves as the effect of different failure-initiating defects sizes and positions is taken into account (Fig. 11c). By using Shiozawa law, the estimated critical defect sizes by traditional as well as ML-assisted EVS can be transformed into fatigue limit or strength for a given number of cycles to failure using:

$$N_f = \sqrt{area} \cdot \left[\frac{\Delta\sigma \cdot \sqrt{\pi \cdot \sqrt{area}} \cdot Y}{K_f'}\right]^{-1/d'} \qquad (13)$$

Or

$$\Delta\sigma = \frac{K_f'}{\sqrt{\pi \cdot \sqrt{area}} \cdot Y} \cdot \left[\frac{N_f}{\sqrt{area}}\right]^{-d'} \qquad (14)$$

Where K_f' and $1/d'$ are fitting parameters ($\sqrt{area}$ expressed in [m]) and are reported in Table 6 for the present AlSi10Mg alloy.

6.2. Application of the ML-improved EVS to anomaly description

Anomaly exceedance curves are the most simple tool for a probabilistic assessment [62,63]. In details, once damage tolerance calculations have allowed to determine the critical defect size $\sqrt{area_{crit}}$, the failure probability is:

$$P_f = \Pr[\sqrt{area} > \sqrt{area_{crit}}] = P_e(\sqrt{area_{crit}}) \qquad (15)$$

where the probability of exceedance for $\sqrt{area_{crit}}$ is calculated for the relevant material volume [64]. Considering Eq. (9) can be calculated as:

$$P_e(x) = 1 - F(x)_{max,V_{ref}} \qquad (16)$$

The impact of the new ML-assisted EVS has been evaluated by determining the anomaly exceedance curves for a prospective material volume by adopting the traditional EVS and the ML-assisted one.

The improvements of the new method are particularly evidenced in Fig. 12, which shows the exceedance curves onto a prospective volume $V_{ref} = 50$ mm^3, realized with the EV distributions for sampling volumes
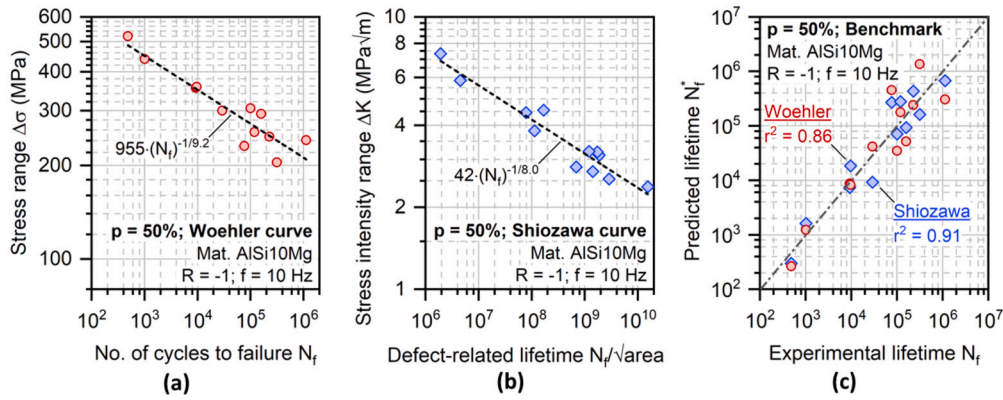
Fig. 11. Assessment of fatigue behavior by: (a) S-N curve according to Woehler, (b) Shiozawa curve and (c) benchmark for coefficients of determination between Woehler and Shiozawa law.
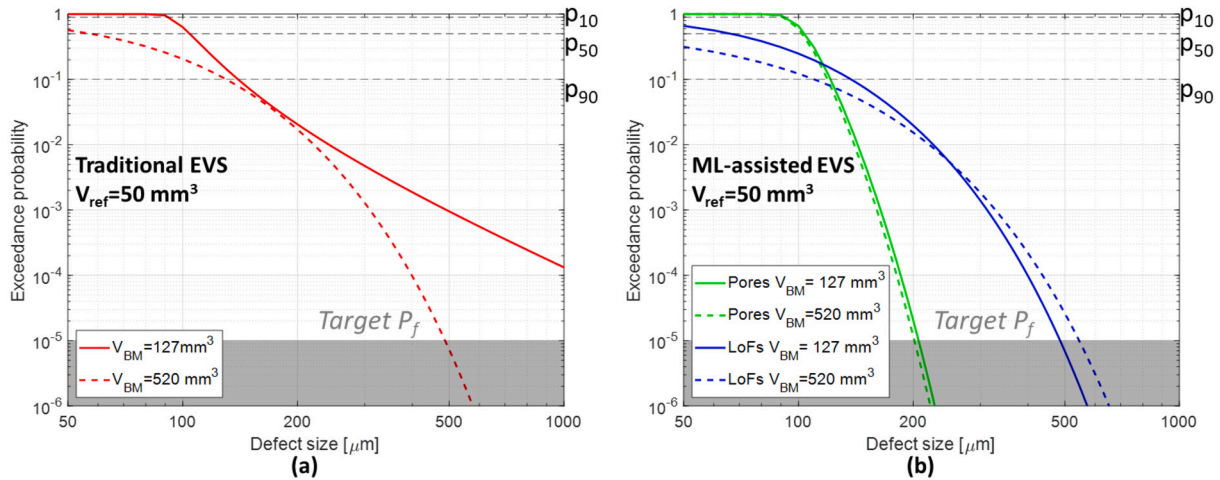

Fig. 12. Comparison of exceedance curves on $V_{ref} = 50$ mm^3 using sampling volumes $V_{BM} = 127$ mm^3 and 520 mm^3 for: (a) traditional method; (b) proposed new route.

$V_{BM} = 127$ mm^3 and 520 mm^3 with the traditional method (Fig. 12(a)) and the proposed new method (Fig. 12(b)).

Typical target failure probabilities are between $P_f = 10^{-5}$ and $P_f = 10^{-6}$ [65] and are shown with a grey area on the exceedance curves. It is possible to see how traditional EVS for $V_{BM} = 127$ mm^3 leads to completely different critical defects in the typical failure probabilities region, compared to $V_{BM} = 520$ mm^3. On the other hand, ML-assisted EVS the predictions are consistent for the two V_{BM}s. The differences evidenced with the traditional EVS may lead to severe underestimation of material strength.

6.3. Prospective fatigue strength distribution

As the defect size is extremely critical in the HCF regime, the $\sqrt{area}$-specific fatigue strength depending on the failure probability was determined for 10^6 cycles and a reference volume $V_{ref} = 50$ mm^3, using the distribution obtained with traditional and ML-assisted EVS onto $V_{BM} = 127$ and 520 mm^3. Fig. 13 shows the computed fatigue strength $\Delta\sigma$ from Shiozawa (Equation (14) with $N_f = 10^6$ and $\sqrt{area}$ expressed in [m]) against the failure probability P_f from the exceedance curves (Equation (16) with $\sqrt{area}$ expressed in [μm]). Both equations are a function of $\sqrt{area}$, thus each point on the diagram implicitly represents a defect size. The single P_f curve shown for the ML-assisted EVS (Fig. 13b) was obtained as the combination of the failure modes by adopting a Weakest Link [65] approach:

$$R = 1 - P_f = R_{pores} \cdot R_{LoFs} \qquad (17)$$

and considering Eq. (16), the failure probability results to be:

$$P_f = 1 - \left(F_{pores}\right)^{\frac{V_{ref}}{V_{BM}}} \cdot \left(F_{LoFs}\right)^{\frac{V_{ref}}{V_{BM}}} \qquad (18)$$

which becomes *competing risk* model as proposed in [35,66].

The traditional EVS for $V_{BM} = 127$ mm^3 leads to a dramatic underestimation of fatigue strength or performance of the material, with a difference of more than 50 MPa from the estimate obtained with $V_{BM} = 520$ mm^3. Using ML-assisted EVS, the gap between different V_{BM}s can be reduced to around 5 MPa. In relation to the fatigue strength the difference is lower than 5% compared to more than 50% gap for traditional EVS, that means a more reliable assessment of critical defects size and fatigue strength for the threshold failure probability (10^{-5} to 10^{-6}) of common regulations [65].

Finally, it is possible to observe how the estimates obtained with traditional EVS for $V_{BM} = 520$ mm^3 and ML-assisted EVS are quite similar, especially in the target failure probability region. This can be attributed to the fact that, for the considered volume $V_{ref} = 50$ mm^3 and for low failure probabilities, the most detrimental defects are the rare defect such as the LoFs, which are well described by the maxima distribution on $V_{BM} = 520$ mm^3.

It is worth remarking that this statement is only valid for $V_{ref} = 50$ mm^3 (and larger volumes), while for much smaller material volumes the presence of pore anomalies becomes the main source of failures. This kind of analysis can be simply done for any V_{ref} by using Eq. (9) and Eq. (17).
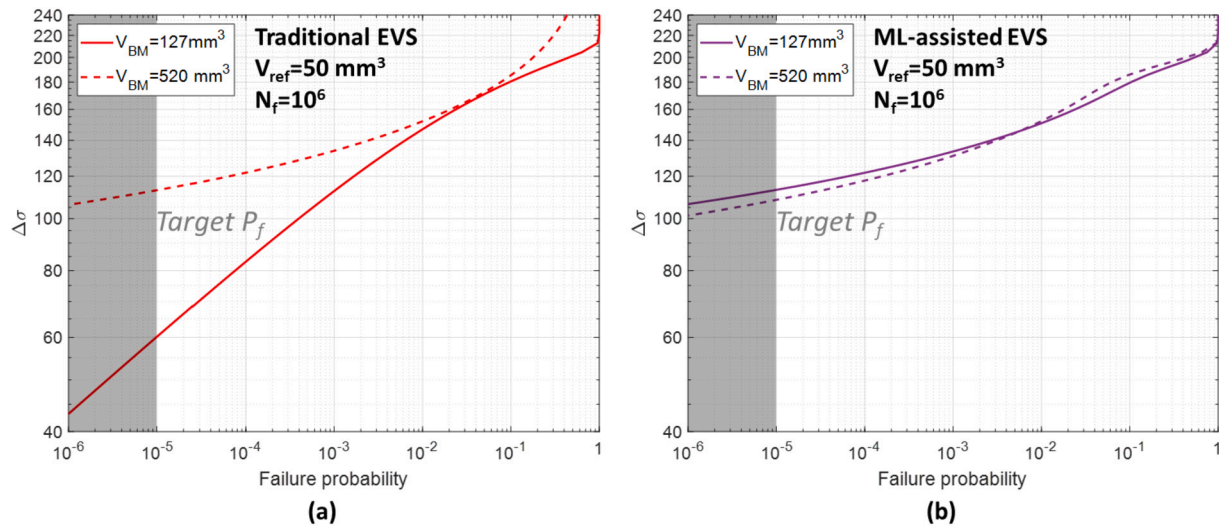
Fig. 13. Estimated fatigue limit $\Delta\sigma$ on $V_{ref} = 50$ mm^3 using Shiozawa and exceedance curves for sampling volumes $V_{BM} = 127$ mm^3 and 520 mm^3 for: (a) traditional method; (b) proposed new route.

7. Conclusions

This work analyzed the CT scans of Alsi10Mg specimens manufactured by L-PBF. The analysis of CT data showed that traditional EVS may produce significant inaccuracies in the estimates of the largest defects in a volume. In fact, the presence of different defect types, observed both on the fracture surfaces and from the CT scan data of HCF specimens, significantly affected the fitting of block maxima sampled defects for different sampling volumes. The limitations of traditional EVS could be overcome by applying supervised machine learning algorithms to classify the defects. Therefore, a new ML-assisted EVS procedure was proposed. Despite the fact that the approach needs a training of the ML algorithm (for given material, process and CT can parameters), the advantages of the procedure are:

- ML-assisted EVS provides stable maxima distributions, unaffected by the sampling volume, unlike the GEVD applied on traditional EVS.
- The stable maxima distributions may be employed to construct robust anomaly exceedance curves for each type of anomaly. For a $V_{ref} = 50$ mm^3, the differences in the region of target failure probability for different sampling volumes are extreme: for traditional EVS the defect size ranges from 500 μm to several mm, while for the ML-assisted EVS the defect size range is from 500 μm to 600 μm.
- The exceedance curves may be used to determine which defect type is more detrimental for different material volumes. For instance, exceedance curves on large material volumes ($V_{ref} \geq 50$ mm^3) showed that rare defects, i.e. lack-of-fusions, were the ones governing the region of target failure probability.
- Provided that fatigue life is propagation dominated, combining the exceedance curves with the Shiozawa curve it is possible to obtain robust fatigue strength predictions. For a $V_{ref} = 50$ mm^3, the difference in fatigue strength prediction for different sampling volumes within the region of target failure probability was less than 5%, while the traditional EVS approach showed a gap of more than 50%.

CRediT authorship contribution statement

Contributions to this paper are as follows: (i) G. Minerva: Experiments, Analysis of results, Draft manuscript, Figure editing (ii) M. Awd: Analysis of results, Draft manuscript (iii) J. Tenkamp: Analysis of results, Draft manuscript, Figure editing (iv) F. Walther: Discussion of results, Manuscript revision (v) S. Beretta: Conceptualization, Project direction, Discussion of results, Manuscript revision

Declaration of competing interest

The authors declare that they have no known competing financial interests or personal relationships that could have appeared to influence the work reported in this paper.

Data availability

Data will be made available on request.

Acknowledgements

References

[1] A. Yadollahi, N. Shamsaei, Additive manufacturing of fatigue resistant materials: challenges and opportunities, Int. J. Fatigue 98 (2017) 14–31, https://doi.org/10.1016/j.ijfatigue.2017.01.001, https://linkinghub.elsevier.com/retrieve/pii/S0142112317300014.

[2] H. Masuo, Y. Tanaka, S. Morokoshi, H. Yagura, T. Uchida, Y. Yamamoto, Y. Murakami, Influence of defects, surface roughness and HIP on the fatigue strength of Ti-6Al-4V manufactured by additive manufacturing, Int. J. Fatigue 117 (2018) 163–179, https://doi.org/10.1016/j.ijfatigue.2018.07.020, https://linkinghub.elsevier.com/retrieve/pii/S0142112318303050.

[3] J. Pegues, M. Roach, R. Scott Williamson, N. Shamsaei, Surface roughness effects on the fatigue strength of additively manufactured Ti-6Al-4V, Int. J. Fatigue 116 (2018) 543–552, https://doi.org/10.1016/j.ijfatigue.2018.07.013, https://linkinghub.elsevier.com/retrieve/pii/S0142112318302986.

[4] L. Barricelli, L. Patriarca, A. du Plessis, S. Beretta, Orientation-dependent fatigue assessment of Ti6Al4V manufactured by L-PBF: size of surface features and shielding effect, Int. J. Fatigue 168 (2023) 107401, https://doi.org/10.1016/j.ijfatigue.2022.107401, https://linkinghub.elsevier.com/retrieve/pii/S014211232200651X.

[5] S. Beretta, M. Gargourimotlagh, S. Foletti, A. du Plessis, M. Riccio, Fatigue strength assessment of "as built" AlSi10Mg manufactured by SLM with different build orientations, Int. J. Fatigue 139 (2020) 105737, https://doi.org/10.1016/j.ijfatigue.2020.105737, https://linkinghub.elsevier.com/retrieve/pii/S0142112320302681.

[6] S. Lee, M. Muhammad, J. Zheng, S. Shao, N. Shamsaei, Locational dependency of additively manufactured parts: effects of surface roughness on fatigue behavior, in: 2021 International Solid Freeform Fabrication Symposium, 2021, pp. 494–505, https://hdl.handle.net/2152/90651.

[7] N. Sanaei, A. Fatemi, Defects in additive manufactured metals and their effect on fatigue performance: a state-of-the-art review, Prog. Mater. Sci. 117 (2021) 100724, https://doi.org/10.1016/J.PMATSCI.2020.100724.

[8] S. Romano, A. Brückner-Foit, A. Brandão, J. Gumpinger, T. Ghidini, S. Beretta, Fatigue properties of AlSi10Mg obtained by additive manufacturing: defect-based modelling and prediction of fatigue strength, Eng. Fract. Mech. 187 (2018) 165–189, https://doi.org/10.1016/j.engfracmech.2017.11.002.

[9] P. Nezhadfar, S. Thompson, A. Saharan, N. Phan, N. Shamsaei, Structural integrity of additively manufactured aluminum alloys: effects of build orientation on microstructure, porosity, and fatigue behavior, Addit. Manuf. 47 (2021) 102292, https://doi.org/10.1016/j.addma.2021.102292, https://linkinghub.elsevier.com/retrieve/pii/S2214860421004528.

[10] M. Teschke, J. Moritz, J. Tenkamp, A. Marquardt, C. Leyens, F. Walther, Defect-based characterization of the fatigue behavior of additively manufactured titanium aluminides, Int. J. Fatigue 163 (2022) 107047, https://doi.org/10.1016/j.ijfatigue.2022.107047, https://linkinghub.elsevier.com/retrieve/pii/S0142112322003127.

[11] F. Sausto, P. Carrion, N. Shamsaei, S. Beretta, Fatigue failure mechanisms for AlSi10Mg manufactured by l-PBF under axial and torsional loads: the role of defects and residual stresses, Int. J. Fatigue 162 (2022) 106903, https://doi.org/10.1016/j.ijfatigue.2022.106903, https://linkinghub.elsevier.com/retrieve/pii/S0142112322001736.

[12] E. Wycisk, A. Solbach, S. Siddique, D. Herzog, F. Walther, C. Emmelmann, Effects of defects in laser additive manufactured Ti-6Al-4V on fatigue properties, Phys. Proc. 56 (2014) 371–378, https://doi.org/10.1016/j.phpro.2014.08.120, https://linkinghub.elsevier.com/retrieve/pii/S187538921400265X.

[13] S. Beretta, S. Romano, A comparison of fatigue strength sensitivity to defects for materials manufactured by AM or traditional processes, Int. J. Fatigue 94 (2017) 178–191, https://doi.org/10.1016/j.ijfatigue.2016.06.020.

[14] A. Tridello, C. Boursier Niutta, M. Rossetto, F. Berto, D. Paolino, Statistical estimation of fatigue design curves from datasets involving failures from defects, Int. J. Fatigue 176 (2023) 107882, https://doi.org/10.1016/j.ijfatigue.2023.107882, https://www.sciencedirect.com/science/article/pii/S0142112323003833.

[15] H. Kitagawa, S. Takahashi, Applicability of fracture mechanics to very small cracks or cracks in the early stage, in: Proceeding of the Second International Conference on Mechanical Behavior of Materials, 1976, pp. 627–631.

[16] T. Shi, J. Sun, J. Li, G. Qian, Y. Hong, Machine learning based very-high-cycle fatigue life prediction of AlSi10Mg alloy fabricated by selective laser melting, Int. J. Fatigue 171 (2023) 107585, https://doi.org/10.1016/j.ijfatigue.2023.107585, https://www.sciencedirect.com/science/article/pii/S0142112323000865.

[17] A. Tognan, E. Salvati, Probabilistic defect-based modelling of fatigue strength for incomplete datasets assisted by literature data, Int. J. Fatigue 173 (2023) 107665, https://doi.org/10.1016/j.ijfatigue.2023.107665, https://www.sciencedirect.com/science/article/pii/S0142112323001664.

[18] E. Maleki, S. Bagherifard, N. Razavi, M. Bandini, A. du Plessis, F. Berto, M. Guagliano, On the efficiency of machine learning for fatigue assessment of post-processed additively manufactured AlSi10Mg, Int. J. Fatigue 160 (2022) 106841, https://doi.org/10.1016/j.ijfatigue.2022.106841, https://www.sciencedirect.com/science/article/pii/S0142112322001165.

[19] M. Awd, S. Münstermann, F. Walther, Effect of microstructural heterogeneity on fatigue strength predicted by reinforcement machine learning, Fatigue Fract. Eng. Mater. Struct. 45 (11) (2022) 3267–3287, https://doi.org/10.1111/ffe.13816, https://onlinelibrary.wiley.com/doi/10.1111/ffe.13816.

[20] H. Bao, S. Wu, Z. Wu, G. Kang, X. Peng, P.J. Withers, A machine-learning fatigue life prediction approach of additively manufactured metals, Eng. Fract. Mech. 242 (2021) 107508, https://doi.org/10.1016/j.engfracmech.2020.107508, https://www.sciencedirect.com/science/article/pii/S0013794420310663.

[21] X. Peng, S. Wu, W. Qian, J. Bao, Y. Hu, Z. Zhan, G. Guo, P.J. Withers, The potency of defects on fatigue of additively manufactured metals, Int. J. Mech. Sci. 221 (2022) 107185, https://doi.org/10.1016/j.ijmecsci.2022.107185, https://www.sciencedirect.com/science/article/pii/S0020740322001102.

[22] E. Salvati, A. Tognan, L. Laurenti, M. Pelegatti, F. De Bona, A defect-based physics-informed machine learning framework for fatigue finite life prediction in additive manufacturing, Mater. Des. 222 (2022) 111089, https://doi.org/10.1016/j.matdes.2022.111089, https://www.sciencedirect.com/science/article/pii/S0264127522007110.

[23] M. Awd, F. Walther, Machine learning of fatigue strength of hybrid and additively manufactured aluminum alloys in VHCF regime, in: Advances in Accelerated Testing and Predictive Methods in Creep, Fatigue, and Environmental Cracking, ASTM International, 100 Barr Harbor Drive, PO Box C700, West Conshohocken, PA 19428-2959, 2023, pp. 262–276, https://www.astm.org/doiLink.cgi?STP164320210096.

[24] M. Awd, L. Saeed, F. Walther, A review on the enhancement of failure mechanisms modeling in additively manufactured structures by machine learning, Eng. Fail. Anal. 151 (2023) 107403, https://doi.org/10.1016/j.engfailanal.2023.107403, https://www.sciencedirect.com/science/article/pii/S1350630723003576.

[25] X. Zhou, N. Dai, M. Chu, L. Wang, D. Li, L. Zhou, X. Cheng, X-ray CT analysis of the influence of process on defect in ti-6Al-4V parts produced with selective laser melting technology, Int. J. Adv. Manuf. Technol. 106 (1–2) (2020) 3–14, https://doi.org/10.1007/s00170-019-04347-0, http://link.springer.com/10.1007/s00170-019-04347-0.

[26] A. du Plessis, I. Yadroitsava, I. Yadroitsev, Effects of defects on mechanical properties in metal additive manufacturing: a review focusing on X-ray tomography insights, Mater. Des. 187 (2020) 108385, https://doi.org/10.1016/j.matdes.2019.108385, https://linkinghub.elsevier.com/retrieve/pii/S0264127519308238.

[27] ECSS Secretariat, ESA-ESTEC Requirements & Standards Division, ECSS-Q-ST-70-80C - Space product assurance - Processing and quality assurance requirements for metallic powder bed fusion technologies for space applications, 2021.

[28] G. Schweiger, K. Heckel, Size effect in randomly loaded specimens, Int. J. Fatigue 8 (4) (1986) 231–234, https://doi.org/10.1016/0142-1123(86)90026-5.

[29] M. Shirani, G. Härkegård, Fatigue life distribution and size effect in ductile cast iron for wind turbine components, Eng. Fail. Anal. 18 (1) (2011) 12–24, https://doi.org/10.1016/j.engfailanal.2010.07.001, https://linkinghub.elsevier.com/retrieve/pii/S1350630710001275.

[30] D.S. Paolino, Very high cycle fatigue life and critical defect size: modeling of statistical size effects, Fatigue Fract. Eng. Mater. Struct. 44 (5) (2021) 1209–1224, https://doi.org/10.1111/ffe.13424, https://onlinelibrary.wiley.com/doi/10.1111/ffe.13424.

[31] Y. Murakami, Inclusion rating by statistics of extreme values and its application to fatigue strength prediction and quality control of materials, J. Res. Natl. Inst. Stand. Technol. 99 (4) (1994).

[32] S. Beretta, L. Patriarca, M. Gargourimotlagh, A. Hardaker, D. Brackett, M. Salimian, J. Gumpinger, T. Ghidini, A benchmark activity on the fatigue life assessment of AlSi10Mg components manufactured by L-PBF, Mater. Des. 218 (2022) 110713, https://doi.org/10.1016/j.matdes.2022.110713, https://linkinghub.elsevier.com/retrieve/pii/S0264127522003355.

[33] P. Kousoulas, Y. Guo, On the probabilistic prediction for extreme geometrical defects induced by laser-based powder bed fusion, CIRP J. Manuf. Sci. Technol. 41 (2023) 124–134, https://doi.org/10.1016/j.cirpj.2022.11.024, https://www.sciencedirect.com/science/article/pii/S1755581722002024.

[34] N. Sanaei, A. Fatemi, N. Phan, Defect characteristics and analysis of their variability in metal L-PBF additive manufacturing, Mater. Des. 182 (2019) 108091, https://doi.org/10.1016/j.matdes.2019.108091.

[35] S. Beretta, More than 25 years of extreme value statistics for defects: fundamentals, historical developments, recent applications, Int. J. Fatigue 151 (2021) 106407, https://doi.org/10.1016/J.IJFATIGUE.2021.106407.

[36] C. Qiu, C. Panwisawas, M. Ward, H.C. Basoalto, J.W. Brooks, M.M. Attallah, On the role of melt flow into the surface structure and porosity development during selective laser melting, Acta Mater. 96 (2015) 72–79, https://doi.org/10.1016/j.actamat.2015.06.004, https://linkinghub.elsevier.com/retrieve/pii/S1359645415003870.

[37] C. Zhao, K. Fezzaa, R.W. Cunningham, H. Wen, F. De Carlo, L. Chen, A.D. Rollett, T. Sun, Real-time monitoring of laser powder bed fusion process using high-speed X-ray imaging and diffraction, Sci. Rep. 7 (1) (2017) 3602, https://doi.org/10.1038/s41598-017-03761-2, https://www.nature.com/articles/s41598-017-03761-2.

[38] C.L.A. Leung, S. Marussi, R.C. Atwood, M. Towrie, P.J. Withers, P.D. Lee, In situ X-ray imaging of defect and molten pool dynamics in laser additive manufacturing, Nat. Commun. 9 (1) (2018) 1355, https://doi.org/10.1038/s41467-018-03734-7, https://www.nature.com/articles/s41467-018-03734-7.

[39] J. Zhang, B. Song, Q. Wei, D. Bourell, Y. Shi, A review of selective laser melting of aluminum alloys: processing, microstructure, property and developing trends, J. Mater. Sci. Technol. 35 (2) (2019) 270–284, https://doi.org/10.1016/j.jmst.2018.09.004, https://linkinghub.elsevier.com/retrieve/pii/S1005030218301804.

[40] A. International, ASTM E3166-20 Standard Guide for Nondestructive Examination of Metal Additively Manufactured Aerospace Parts After Build, 2020.

[41] G. Kasperovich, J. Haubrich, J. Gussone, G. Requena, Correlation between porosity and processing parameters in TiAl6V4 produced by selective laser melting, Mater. Des. 105 (2016) 160–170, https://doi.org/10.1016/j.matdes.2016.05.070, https://linkinghub.elsevier.com/retrieve/pii/S0264127516306761.

[42] R. Snell, S. Tammas-Williams, L. Chechik, A. Lyle, E. Hernández-Nava, C. Boig, G. Panoutsos, I. Todd, Methods for rapid pore classification in metal additive manufacturing, JOM 72 (1) (2020) 101–109, https://doi.org/10.1007/s11837-019-03761-9, http://link.springer.com/10.1007/s11837-019-03761-9.

[43] A. Poudel, M.S. Yasin, J. Ye, J. Liu, A. Vinel, S. Shao, N. Shamsaei, Feature-based volumetric defect classification in metal additive manufacturing, Nat. Commun. 13 (1) (2022) 6369, https://doi.org/10.1038/s41467-022-34122-x, https://www.nature.com/articles/s41467-022-34122-x.

[44] J. Ye, A. Poudel, J. Liu, A. Vinel, D. Silva, S. Shao, N. Shamsaei, Machine learning augmented X-ray computed tomography features for volumetric defect classification in laser beam powder bed fusion, Int. J. Adv. Manuf. Technol. 126 (7–8) (2023) 3093–3107, https://doi.org/10.1007/s00170-023-11281-9, https://link.springer.com/10.1007/s00170-023-11281-9.

[45] M. Vandecasteele, R. Heylen, D. Iuso, A. Thanki, W. Philips, A. Witvrouw, D. Verhees, B.G. Booth, Towards material and process agnostic features for the classification of pore types in metal additive manufacturing, Mater. Des. 227 (2023) 111757, https://doi.org/10.1016/j.matdes.2023.111757, https://linkinghub.elsevier.com/retrieve/pii/S0264127523001727.

[46] M.L. Altmann, T. Benthien, N. Ellendt, A. Toenjes, Defect classification for additive manufacturing with machine learning, Materials 16 (18) (2023), https://doi.org/10.3390/ma16186242, https://www.mdpi.com/1996-1944/16/18/6242.

[47] V. Graphics, 2020, VGStudio MAX 3.4.2 Reference Manual.

[48] S. Datta, J.P. Davim (Eds.), Machine Learning in Industry, Management and Industrial Engineering, Springer International Publishing, Cham, 2022, https://link.springer.com/10.1007/978-3-030-75847-9.

[49] C. Bussler, D. Fensel (Eds.), Artificial Intelligence: Methodology, Systems, and Applications 11th International Conference, AIMSA 2004 Varna, Bulgaria, September 2-4, 2004 Proceedings, Springer, Berlin, Heidelberg, 2004.

[50] Y. Murakami, Metal Fatigue: Effects of Small Defects and Nonmetallic Inclusions, Academic Press, 2019.

[51] S. Romano, A. Brandão, J. Gumpinger, M. Gschweitl, S. Beretta, Qualification of AM parts: extreme value statistics applied to tomographic measurements, Mater. Des. 131 (2017) 32–48, https://doi.org/10.1016/j.matdes.2017.05.091.

[52] R.L. Smith, Extreme value theory, in: Handbook of Applicable Mathematics, vol. 7, 1990, pp. 437–471.

[53] S. Coles, An Introduction to Statistical Modeling of Extreme Values, Springer Series in Statistics, Springer London, London, 2001.

[54] S. Beretta, Affidabilità delle costruzioni meccaniche: Strumenti e metodi per l'affidabilità di un progetto, Springer Science & Business Media, 2010.

[55] ASTM, ASTM E2283-03 Standard Practice for Extreme Value Analysis of Nonmetallic Inclusions in Steels and Other Microstructural Features, American Society for Testing and Materials, 2003.

[56] S. Romano, A. Abel, J. Gumpinger, A.D. Brandão, S. Beretta, Quality control of AlSi10Mg produced by SLM: metallography versus CT scans for critical defect size assessment, Addit. Manuf. 28 (February) (2019) 394–405, https://doi.org/10.1016/j.addma.2019.05.017.

[57] Y. Murakami, Material defects as the basis of fatigue design, Int. J. Fatigue 41 (2012) 2–10, https://doi.org/10.1016/j.ijfatigue.2011.12.001, https://linkinghub.elsevier.com/retrieve/pii/S0142112311003161.

[58] A. Yadollahi, M.J. Mahtabi, A. Khalili, H.R. Doude, J.C. Newman, Fatigue life prediction of additively manufactured material: effects of surface roughness, defect size, and shape, Fatigue Fract. Eng. Mater. Struct. (2018), https://doi.org/10.1111/ffe.12799.

[59] K. Shiozawa, L. Lu, Effect of non-metallic inclusion size and residual stresses on gigacycle fatigue properties in high strength steel, Adv. Mater. Res. 44–46 (2008) 33–42, https://doi.org/10.4028/www.scientific.net/AMR.44-46.33, https://www.scientific.net/AMR.44-46.33.

[60] J. Tenkamp, F. Stern, F. Walther, Uniform fatigue damage tolerance assessment for additively manufactured and cast Al-Si alloys: an elastic-plastic fracture mechanical approach, Addit. Manuf. Lett. 3 (2022) 100054, https://doi.org/10.1016/j.addlet.2022.100054, https://linkinghub.elsevier.com/retrieve/pii/S2772369022000287.

[61] J. Tenkamp, S. Stammkötter, F. Walther, Qualification of uniform fatigue damage tolerance law for additively manufactured and cast Al-Si alloys, Procedia Struct. Integr. 42 (2022) 328–335, https://doi.org/10.1016/j.prostr.2022.12.040, https://linkinghub.elsevier.com/retrieve/pii/S2452321622005972.

[62] R. Corran, M. Gorelik, D. Lehmann, S. Mosset, The development of anomaly distributions for machined holes in aircraft engine rotors, in: Volume 5: Marine; Microturbines and Small Turbomachinery; Oil and Gas Applications; Structures and Dynamics, Parts A and B, ASMEDC, 2006, pp. 941–950, https://asmedigitalcollection.asme.org/GT/proceedings/GT2006/42401/941/315592.

[63] R.S.J. Corran, M. Gorelik, D. Chawla, S. Mosset, M.B. Joinson, D. Harmon, D. Nissley, A.J. Murphy, J. Stillinger, K.W. Jacques, Review of probabilistic damage tolerance methodology for hard alpha anomalies, in: Volume 7: Structures and Dynamics, Parts A and B, American Society of Mechanical Engineers, 2012, pp. 397–406, https://asmedigitalcollection.asme.org/GT/proceedings/GT2012/44731/397/247772.

[64] FAA, AC 33.14-1 damage tolerance for high, Energy Turbine Engine Rotors (2017).

[65] FAA, AC 33.70-2 Damage Tolerance of Hole Features in High-Energy Turbine, 2008.

[66] S. Beretta, C. Anderson, Y. Murakami, Extreme value models for the assessment of steels containing multiple types of inclusion, Acta Mater. 54 (8) (2006) 2277–2289, https://doi.org/10.1016/j.actamat.2006.01.016, https://linkinghub.elsevier.com/retrieve/pii/S1359645406000814.